JAMES | Journal of Advances in Modeling Earth Systems

RESEARCH ARTICLE
10.1029/2024MS004315

Improved Precipitation Diurnal Cycle in GFDL Climate Models With Non-Equilibrium Convection

Bosong Zhang[1], Leo J. Donner[2], Ming Zhao[2], and Zhihong Tan[1]

[1]Program in Atmospheric and Oceanic Sciences, Princeton University, Princeton, NJ, USA, [2]NOAA/Geophysical Fluid Dynamics Laboratory, Princeton, NJ, USA

Key Points:

- A new convective closure is applied to Geophysical Fluid Dynamics Laboratory's CMIP6 climate models AM4 (atmosphere-only) and CM4 (ocean-atmosphere coupled)
- The diurnal cycle of precipitation is significantly improved over land
- The new closure does not significantly change many aspects of AM4 and CM4's mean state and variability aside from their diurnal precipitation cycles

Correspondence to:
B. Zhang,
bosongzhang@gmail.com

Citation:
Zhang, B., Donner, L. J., Zhao, M., & Tan, Z. (2024). Improved precipitation diurnal cycle in GFDL climate models with non-equilibrium convection. *Journal of Advances in Modeling Earth Systems*, *16*, e2024MS004315. https://doi.org/10.1029/2024MS004315

Received 1 MAR 2024
Accepted 6 AUG 2024

Abstract Most global climate models with convective parameterization have trouble in simulating the observed diurnal cycle of convection. Maximum precipitation usually happens too early during summertime, especially over land. Observational analyses indicate that deep convection over land cannot keep pace with rapid variations in convective available potential energy, which is largely controlled by boundary-layer forcing. In this study, a new convective closure in which shallow and deep convection interact strongly, out of equilibrium, is implemented in atmosphere-only and ocean-atmosphere coupled models. The diurnal cycles of convection in both simulations are significantly improved with small changes to their mean states. The new closure shifts maximum precipitation over land later by about three hours. Compared to satellite observations, the diurnal phase biases are reduced by half. Shallow convection to some extent equilibrates rapid changes in the boundary layer at subdiurnal time scales. Relaxed quasi-equilibrium for convective available potential energy holds in significant measure as a result. Future model improvement will focus on the remaining biases in the diurnal cycle, which may be further reduced by including stochastic entrainment and cold pools.

Plain Language Summary In this study, we tackled a common challenge in general circulation models concerning the timing of intense rainfall over land during summertime. Many models tend to predict the peak of precipitation too early in the day. To address this, our study introduced a new approach to simulate convection by accounting for the role of shallow convection in stabilizing rapid changes in the atmospheric boundary layer at shorter time scales. This approach delayed maximum precipitation over land by approximately three hours. This adjustment significantly improved the simulated precipitation, aligning them more closely with observations from satellite data. Overall, our research contributes to improving numerical models, bringing them closer to accurately simulating the intricate dynamics of convection and precipitation over land.

1. Introduction

Cumulus parameterization is a key component of general circulation models (GCMs). It connects the intensity and vertical structure of sub-grid scale convection with the grid column mean state. Arakawa and Schubert (1974) argued that convection is in quasi-equilibrium, as measured by cloud work function (CWF), closely related to convective available potential energy (CAPE), with forcing due to large-scale processes like advection and radiation. For time scales of order 1 day and beyond, quasi-equilibrium has proved valid based on both theoretical and experimental studies (Jones & Randall, 2011; Neelin & Yu, 1994; Yano & Plant, 2012). However, processes in the planetary boundary layer (PBL) usually exhibit shorter time scales than processes in the free troposphere (Donner & Phillips, 2003; Raymond & Herman, 2011; Zhang, 2002), challenging quasi-equilibrium on these shorter time scales.

Convective heat sources, moisture sinks, precipitation, and tracer transports are closely related to convective mass fluxes. The vertical profiles of the mass fluxes are typically determined by using plume models, with the base mass flux determined by a closure. Several convection parameterization schemes following the mass-flux framework have been developed to simulate "equilibrium convection" (Arakawa & Schubert, 1974; Donner et al., 2001; Emanuel, 1991; Kain & Fritsch, 1993; Tiedtke, 1989; Zhang & McFarlane, 1995). These schemes show varied abilities in simulating tropical waves and intraseasonal variability (Kim et al., 2011; Lin et al., 2006). The quasi-equilibrium assumption used in the European Centre for Medium-Range Weather Forecasts (ECMWF) Integrated Forecasting System (IFS) is found to reproduce reasonably well the observed mid-latitude synoptic variability, tropical wave spectra and intraseasonal variability (Bechtold et al., 2008; Hirons et al., 2013).

In contrast to equilibrium convection, non-equilibrium convection often holds at time scales of several hours (Davies et al., 2013; Jones & Randall, 2011; Yano & Plant, 2012). Non-equilibrium convection usually occurs in the presence of strong free troposphere forcing or surface heat fluxes. During summertime, surface heat fluxes over land are largely modulated by solar insolation. Variations in surface heat fluxes drive rapid changes in CAPE with which convection is out of equilibrium, as is the related strong diurnal cycle of precipitation over land. Overall, the diurnal cycle of convection over land is characterized by shallow convection in the morning with precipitation associated with deep convection peaking in the late afternoon to early evening (Dai et al., 1999; Tian et al., 2005). It is challenging for state-of-art GCMs to correctly simulate the observed diurnal cycle of precipitation over land. Model-simulated maximum precipitation over land usually happens too early and its phase closely follows the phase of surface fluxes that are largely determined by solar radiation (Christopoulos & Schneider, 2021; Dong, Krasting, & Guo, 2023; Stratton & Stirling, 2012; Tao et al., 2024; Zhao et al., 2018b). While coarse-resolution GCMs struggle in simulating the observed diurnal cycle of convection, the observed diurnal cycle can be simulated reasonably in cloud resolving models with resolutions of order 2.5 km or higher (Petch et al., 2002; Stirling & Stratton, 2012). This study addresses convective parameterization in coarse-resolution GCMs.

Apart from resolution, previous studies have explored various strategies to improve the diurnal cycle of convection, including but not limited to entrainment rates (Del Genio & Wu, 2010; Piriou et al., 2007; Stratton & Stirling, 2012), a prognostic closure accounting for convective memory (Gerard et al., 2009; Pan & Randall, 1998), convective closures including convective inhibition and cold pools (Fletcher & Bretherton, 2010; Mapes, 2000; Rio et al., 2009), a convective triggering function (Xie et al., 2019), and humidity (Fuchs & Raymond, 2007). However, these approaches have not proved to be universally suited for GCMs. An alternate strategy is suggested by observational analyses showing that CAPE variability is controlled by boundary-layer variability, emphasized by Donner and Phillips (2003) and consistent with analyses by Zhang (2002, 2003). In light of this, Bechtold et al. (2014) proposed augmenting the relaxed quasi-equilibrium closure often used for deep convection by a non-equilibrium term accounting for the inability of deep convection to equilibrate CAPE changes resulting from rapid non-convective PBL processes. Improvements in the ECMWF IFS diurnal cycle using this closure encouraged us to explore non-equilibrium convection in the Geophysical Fluid Dynamics Laboratory (GFDL) climate models.

In this study, we show that including non-equilibrium, shallow convection in the closure for deep convection significantly improves the simulation of the diurnal cycle in GFDL AM4 (atmosphere) (Zhao et al., 2018a, 2018b) and CM4 (coupled ocean-atmosphere) (Held et al., 2019) models, while still leaving a notable bias. Section 2 describes the non-equilibrium closure for deep convection. Section 3 shows that changing the deep convection closure in AM4 and CM4 improves diurnal precipitation cycles while changing only slightly other key simulation characteristics. In Section 4 we summarize and suggest possible further ways to improve simulation of the diurnal cycle of convection. In Appendix A, we relate this closure based on relaxed quasi-equilibrium including both deep and shallow (non-equilibrium) convection to a non-equilibrium closure in which CAPE changes are controlled by non-convective PBL processes. We show that shallow convection responds strongly to changes produced by rapid non-convective PBL processes. In the limit where shallow convection equilibrates non-convective PBL processes, the two non-equilibrium closures are identical.

2. Method and Experiments

2.1. Non-Equilibrium Convection

An established method for parameterizing convection is balancing CAPE or CWF changes produced by deep convection with a relaxation of CAPE or CWF changes by non-convective processes, notably large-scale advection, surface fluxes, radiative cooling, and eddy diffusion (Moorthi & Suarez, 1992; Zhang & McFarlane, 1995). Several generations of GFDL climate models have adopted this approach (Anderson et al., 2004; Donner et al., 2011; Zhao et al., 2018a), and all have suffered from large biases in their diurnal cycles of precipitation, mostly over land but also to a lesser degree over ocean. Based on observational analysis showing this balance does not hold at sub-diurnal time scales (Donner & Phillips, 2003; Zhang, 2002, 2003), we generalize this balance to include non-equilibrium convection. The processes changing CAPE are:

$$\left(\frac{\partial CAPE}{\partial t}\right) = \left(\frac{\partial CAPE}{\partial t}\right)_{nc,BL} + \left(\frac{\partial CAPE}{\partial t}\right)_{nc,FT} + \left(\frac{\partial CAPE}{\partial t}\right)_{deep} + \left(\frac{\partial CAPE}{\partial t}\right)_{shal} \quad (1)$$

Here, the subscript "nc" refers to all non-convective processes. "BL" refers to changes in the PBL, while changes in the overlying free troposphere are denoted by "FT." These tendencies are easily computed in a model using tendencies from the dynamical core and parameterizations for radiative transfer, surface fluxes, and sub-grid diffusion. The subscripts "deep" and "shal" refer to CAPE changes from deep and shallow convection, respectively.

Quasi-equilibrium (Arakawa & Schubert, 1974) has been proposed as a closure for convective mass fluxes, to which are related convective heat sources, moisture sinks, precipitation, and tracer transport. Quasi-equilibrium posits:

$$\left(\frac{\partial CAPE}{\partial t}\right) \ll \left(\frac{\partial CAPE}{\partial t}\right)_{nc,BL} + \left(\frac{\partial CAPE}{\partial t}\right)_{nc,FT} \quad (2)$$

when Equation 2 holds, convective CAPE tendencies balance non-convective CAPE tendencies. The convective mass fluxes are then obtained from the convective CAPE tendencies. Observations show that quasi-equilibrium is a reasonable approximation as diurnal time scales are approached but does not hold for sub-diurnal time scales (Donner & Phillips, 2003, Fig. 2). A recourse is to relax the non-convective terms in Equation 1:

$$\left(\frac{\partial CAPE}{\partial t}\right)_{nc,BL} + \left(\frac{\partial CAPE}{\partial t}\right)_{nc,FT} = \frac{CAPE - CAPE_0}{\tau} \quad (3)$$

In Equation 3, $CAPE_0$ is a reference value toward which CAPE, having evolved by non-convective processes since its last adjustment due to convection (the beginning of a model time step in AM4), relaxes over an extended time τ. The value of τ is typically tuned to multiple hours in models. Based on field experiments, Donner and Phillips (2003) estimated $CAPE_0$ to be 0 J kg^{-1}, and τ to be 6.5 hr. Zhao et al. (2018b) tuned these to 10 J kg^{-1} and 8 hr, respectively, in AM4.

The relaxed CAPE tendency is then assumed to be in quasi-equilibrium with convective tendencies, implying:

$$\left(\frac{\partial CAPE}{\partial t}\right)_{deep} = -\frac{CAPE - CAPE_0}{\tau} - \left(\frac{\partial CAPE}{\partial t}\right)_{shal} \quad (4)$$

In GFDL AM2, AM3, and AM4, the contribution from non-equilibrium shallow convection has not been included in the determination of the deep convective CAPE tendency and mass fluxes. Rather, only deep convection has been assumed to be in relaxed equilibrium with non-convective tendencies. Shallow convective tendencies are likely to be non-equilibrium and tied closely to the evolution of the PBL. In GFDL AM3 and AM4, shallow convective base mass fluxes M_{shal} follow Bretherton et al. (2004):

$$M_{shal} \propto \sqrt{c_1 TKE}\ exp\left(-\frac{c_2 CIN}{TKE}\right) \quad (5)$$

where TKE denotes PBL turbulent kinetic energy; CIN, convective inhibition; and c_1 and c_2 denote constants. $\left(\frac{\partial CAPE}{\partial t}\right)_{shal}$ in Equation 4 depends strongly on M_{shal}. We hypothesize that non-equilibrium shallow convection and its diurnal cycle are important in the relaxed balance in Equation 4. By removing enthalpy and moisture from the boundary layer, shallow convection generally reduces CAPE (Figures A1a, A1b and A2a, A2b), though infrequent exceptions of small magnitude can occur, for example, for a PBL cold and dry relative to the free troposphere above.

2.2. Observations and Implementation in AM4 and CM4

For observations, we use the NASA Global Precipitation Measurement (GPM) Integrated Multisatellite Retrievals for GPM (IMERG) (Huffman et al., 2015) to evaluate the models' ability in simulating the diurnal cycle of precipitation. IMERG provides a global-gridded product with 0.1° horizontal resolution and 30-min frequency. For a direct comparison with AM4 and CM4 outputs, the IMERG product is re-gridded to 1.0° latitude × 1.25° longitude resolution. In addition, Global Precipitation Climatology Project (GPCP v3.2) (Huffman et al., 2022) is used to evaluate the mean precipitation climatology. The high-frequency IMERG observations are well-suited for evaluating the diurnal cycle, while the combination of surface and satellite observations in GPCP are better suited for evaluation of long-term means. Radiation at the top of the atmosphere from CERES EBAF Edition 4.1 (Loeb et al., 2018) is used to evaluate the models' energy budget. Monthly ERA5 data (Hersbach et al., 2020) is used for temperature comparisons.

AM4 with prescribed sea surface temperatures (SSTs) and sea ice, and pre-industrial (PI) CM4 ocean-atmosphere coupled model are used to explore the effects of non-equilibrium convection. Detailed descriptions of AM4 can be found in Zhao et al. (2018a, 2018b), and CM4 is documented in Held et al. (2019). In both AM4 and CM4, the atmosphere component has 33 vertical levels with a horizontal resolution of approximately 100 km. The PI configuration of CM4 is chosen because the PI period is in global energy balance (unlike present day), rendering an evaluation of PI model drift and energy cycle more straightforward than for an evolving historical simulation, which would, in any case, need to start from a realistic, balanced PI simulation.

We implement a non-equilibrium closure based on Equation 4 including the CAPE tendency due to shallow convection and examine its impact on the diurnal cycle of precipitation in AM4 and CM4 in subsequent sections. Default configurations of the standard AM4 documented in Zhao et al. (2018a, 2018b) used a relaxed quasi-equilibrium closure where CWF changes induced by deep convection are balanced by a relaxation of CWF changes due to non-convective processes. Here, we implement relaxed quasi-equilibrium using CAPE instead of CWF (Equations 3 and 4). Doing so facilitates computations of changes with respect to state changes, which are easily done for CAPE but require additional convective plume calculations for CWF.

CAPE in Equation 4 is calculated using temperature and humidity profiles, as in Eq. (5.8) in Donner (2024). (In that equation, the CWF becomes CAPE when a plume is non-entraining.) The temperature and humidity profiles for the relaxed CAPE term in Equation 4 have been incremented during the model time step by non-convective processes, that is, advection, radiation, surface fluxes, and sub-grid diffusion. Convective mass fluxes in AM4 change the large-scale flow through convergence and divergence of sub-grid fluxes of thermodynamic, dynamic, moisture, and tracer fields, along with corresponding sources and sinks inside the mass fluxes (Eqs. (5.1–5.3) in Donner (2024)). The flux convergence and divergence can equivalently be expressed in terms of convective mass fluxes (Eq. (5.4–5.5) in Donner (2024)), enabling the time evolution of large-scale fields due to convection to be expressed in terms of plume properties and convective mass fluxes (Eq. (5.6) in Donner (2024)). The shallow convective mass flux from Equation 5 results in time tendencies of temperature and humidity, which are then used to evaluate the CAPE tendency due to shallow convection $\left(\frac{\partial \overline{CAPE}}{\partial t}\right)_{shal}$ in Equation 4. By calculating deep plume properties and applying a unit mass flux M_0, large-scale deep convective tendencies of temperature and humidity are obtained, and these are in turn used to determine the relationship between CAPE and the deep convective-base mass flux M_b. Equation 4 implies a change in CAPE due to deep convection, resulting from changes in CAPE from shallow (non-equilibrium) convection and from relaxed non-convective changes in CAPE. The requisite deep convective mass flux is obtained by dividing this CAPE change by $\frac{\partial CAPE}{\partial M_b}$ for deep convection.

Details on the AM4 deep and shallow plumes are provided in Zhao et al. (2018b). Deep convection occurs in AM4 when (a) column relative humidity exceeds a threshold (0.4), (b) CWF (or CAPE, for non-equilibrium convection) exceeds a threshold (10 J kg^{-1}), and (c) plume launched in the PBL can become buoyant, with low-level lifting in the plume augmented when convective gustiness (related to evaporation of convective precipitation) exceeds a threshold. Shallow convection occurs in AM4 when the mass flux in Equation 5 exceeds a minimum which can be determined from Eq. (26) in Bretherton et al. (2004). Shallow and deep convection can occur simultaneously. Indeed, their interplay is essential to the behavior of AM4 non-equilibrium convection. In Equation 4, the shallow and deep CAPE tendencies are both calculated over a model time step.

In this study, the CWF based quasi-equilibrium closure is referred to as standard AM4. The CAPE based non-equilibrium closure based on Equation 4 including the CAPE tendency due to shallow convection is referred

Table 1
Experiments and Observations

Data source	Experiment name	Resolution	Time
AM4	Standard AM4	1.0° lat × 1.25° lon	Prescribed SSTs (Rayner et al., 2003) from 1979 to 2014
	relax QE D+S		
CM4	PI-Control		200 years
	PI relax QE D+S		
Observation	IMERG	0.1° original and re-gridded to 1.0° lat, 1.25° lon	2001 to 2014
	GPCP v3.2	2.5° lat × 2.5° lon	2001 to 2014
	CERES EBAF Edition 4.1	1.0° lat × 1.0° lon	2001 to 2014
	ERA5	0.25° lat × 0.25° lon	2001 to 2014

to as relax QE D+S. Two parameters are retuned in relax QE D+S from those in standard AM4. The retuning simulates Earth's energy imbalance in the relax QE D+S AMIP integration (2001–2014) to a value of 1.08 W/m^2, close to CERES EBAF (0.88 W/m^2). The retuned parameters (a) increase ice fall speeds by 10% and (b) change cloud-top entrainment in stratiform clouds to increase absorbed shortwave radiation (SWABS) at top of the atmosphere (TOA). For CM4, the PI-Control simulation uses the quasi-equilibrium closure based on CWF. The PI simulation using the CAPE based non-equilibrium closure based on Equation 4, with the same two retuned parameters, is referred to as PI relax QE D+S. Table 1 lists the experiments and observational products.

Bechtold et al. (2014) provide an alternate interpretation for non-equilibrium convection. Its incorporation in the ECMWF IFS improved its diurnal precipitation cycle. Appendix A shows the approach here, when implemented in AM4, is closely related.

3. Results

3.1. Diurnal Precipitation Cycle in AM4

To quantify the diurnal amplitude and phase of precipitation, the model outputs and satellite observations are first composited in hourly bins. A Fourier analysis is then applied to the hourly-binned data to get its first harmonic. Figure 1 compares the diurnal amplitude of boreal summer precipitation between IMERG, standard AM4 and relax QE D+S. The observed spatial distribution of diurnal amplitude shows notable peaks over central America, northern Amazon, central Africa, south Asia, and Maritime Continent.

The diurnal phase (local solar time, LST) is shown in Figure 2. For IMERG, maximum precipitation over land occurs mostly from late afternoon to early evening. Over tropical oceans, maximum precipitation predominantly occurs in early morning, although certain regions, such as the Gulf of Mexico and coastal regions off central America and south Asia, exhibit peak precipitation in late morning to local noon (Figure 2a). The largest phase errors in standard AM4 are generally over land. Maximum precipitation over land in standard AM4 occurs around local noon (Figure 2b), which is too early compared to IMERG and is a known issue in AM4 (Zhao et al., 2018a). In relax QE D+S, the diurnal cycle over land is delayed by about three hours relative to standard AM4 (Figure 2c), which means the phase biases between standard AM4 and IMERG are reduced by half. The significant improvement indicates that shallow convection strongly mediates rapid variations in CAPE at subdiurnal time scales consistent with observational analyses shown in Donner and Phillips (2003). The retuning of relax QE D+S discussed in Section 2 does not change Figure 2 noticeably (not shown).

Next, we focus on the diurnal cycle over the contiguous United States during boreal summer (CONUS; Figure 3). The observed diurnal amplitude shows peaks eastward of the Rocky Mountains area and over the southeast CONUS and the corresponding coastal regions (Figure 3a). Standard AM4 reasonably reproduces the diurnal amplitude over the southeast CONUS but underestimates the diurnal amplitude east of the Rocky Mountains (Figure 3b).

The patterns of the diurnal amplitude are overall similar between standard AM4 and relax QE D+S, although some minor improvement is discernible with relax QE D+S over the Sahel (Figure 1) and central America (Figure 3). Consistent small changes in OLR (Figure 8) and SWABS (Figure 9) are mostly evident in these regions.

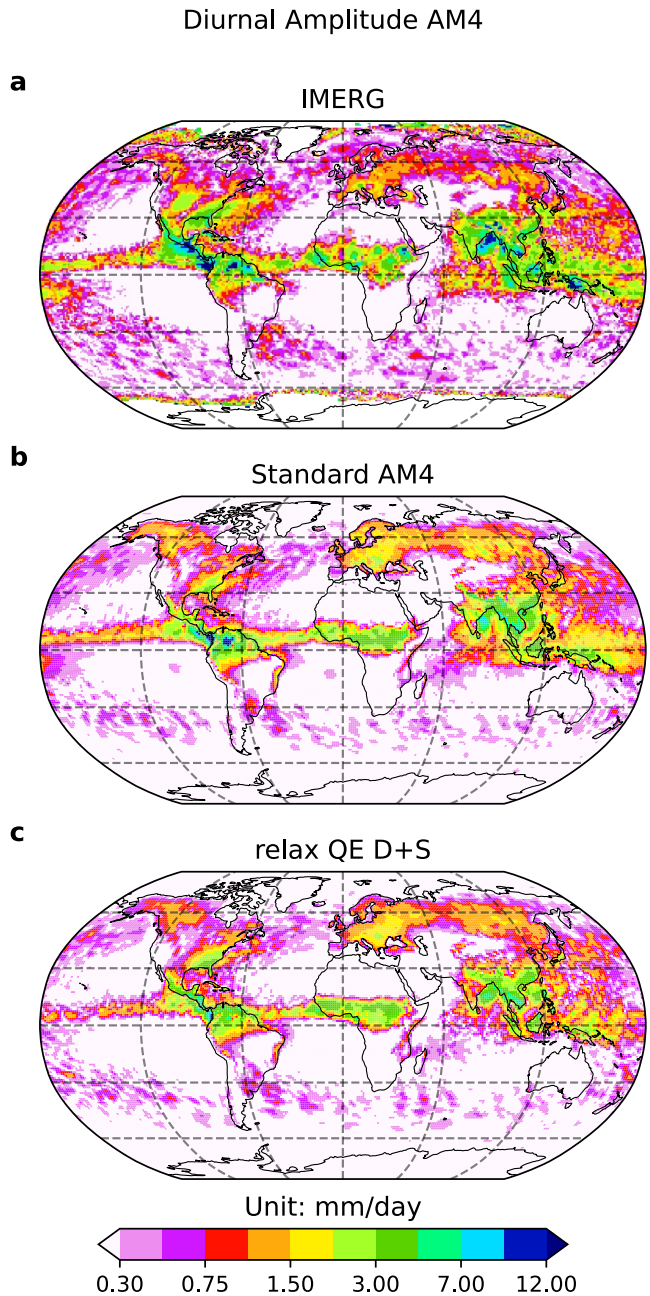

Figure 1. Diurnal amplitude of precipitation (unit: mm day^{-1}) during boreal summer (June-August) for (a) IMERG, (b) Standard AM4, and (c) relax QE D+S.

For the diurnal phase, the observed spatial pattern in IMERG is characterized predominantly by late afternoon convection over the western and eastern United States, and nighttime convection over Central Plains due to mesoscale convective systems (Figure 4a), which is consistent with previous results (Bechtold et al., 2014; Dai et al., 1999; Dong, Zhao, et al., 2023; Tian et al., 2005; Watters et al., 2021). The diurnal phase in standard AM4 is significantly biased from IMERG with maximum precipitation occurring around local noon in most parts of CONUS (Figure 4b). By including the modulation of CAPE by shallow convection in the closure for deep convection, relax QE D+S shifts the diurnal cycle later by about three hours. The diurnal phase is also improved over the surrounding ocean, especially the Gulf of Mexico and coastal regions off the southeast CONUS (Figure 4c). Bechtold et al. (2014) showed similar improvement of the diurnal cycle, globally and over CONUS, with non-equilibrium convection implemented in the ECMWF IFS (their Figures 2 and 4), also with small

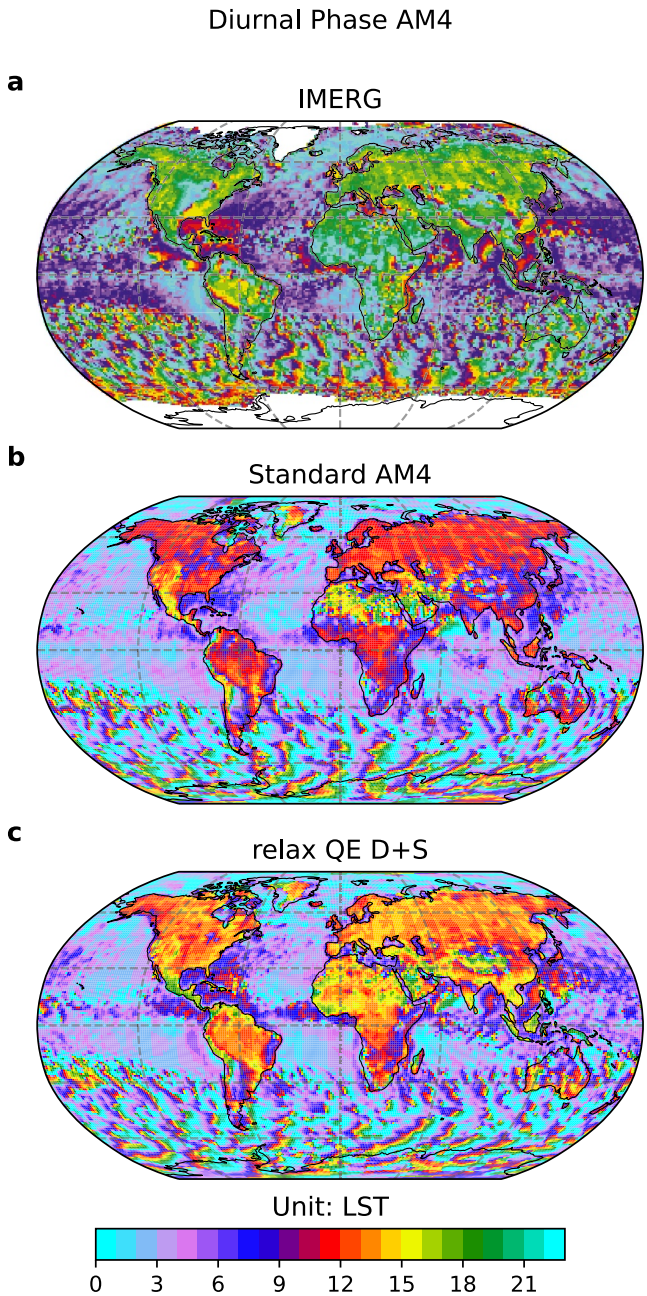

Figure 2. Diurnal phase (unit: LST hour) during boreal summer (June-August) for (a) IMERG, (b) Standard AM4, and (c) relax QE D+S.

changes in CONUS amplitudes (their Figure 3). This suggests the closure based on Equation 4 may be related to the non-equilibrium closure implemented in Bechtold et al. (2014). Appendix A discusses this in detail.

The improved diurnal cycle is further confirmed by domain-averaged precipitation without projection onto a single harmonic. The overall improvement over land areas holds globally (Figure 5a) and at regional scales (Figures 5b–5f). Compared to standard AM4, relax QE D+S weakens convective activity around local noon time but enhances it during late afternoon and early evening. The extent to which the diurnal cycle improves varies with location. For example, the diurnal cycle over the western United States shows less improvement than over the eastern United States. One possible reason is that AM4 with coarse horizontal resolutions is not able to simulate well mesoscale connective systems east of the Rocky Mountains indicated by Figure 3. Similarly,

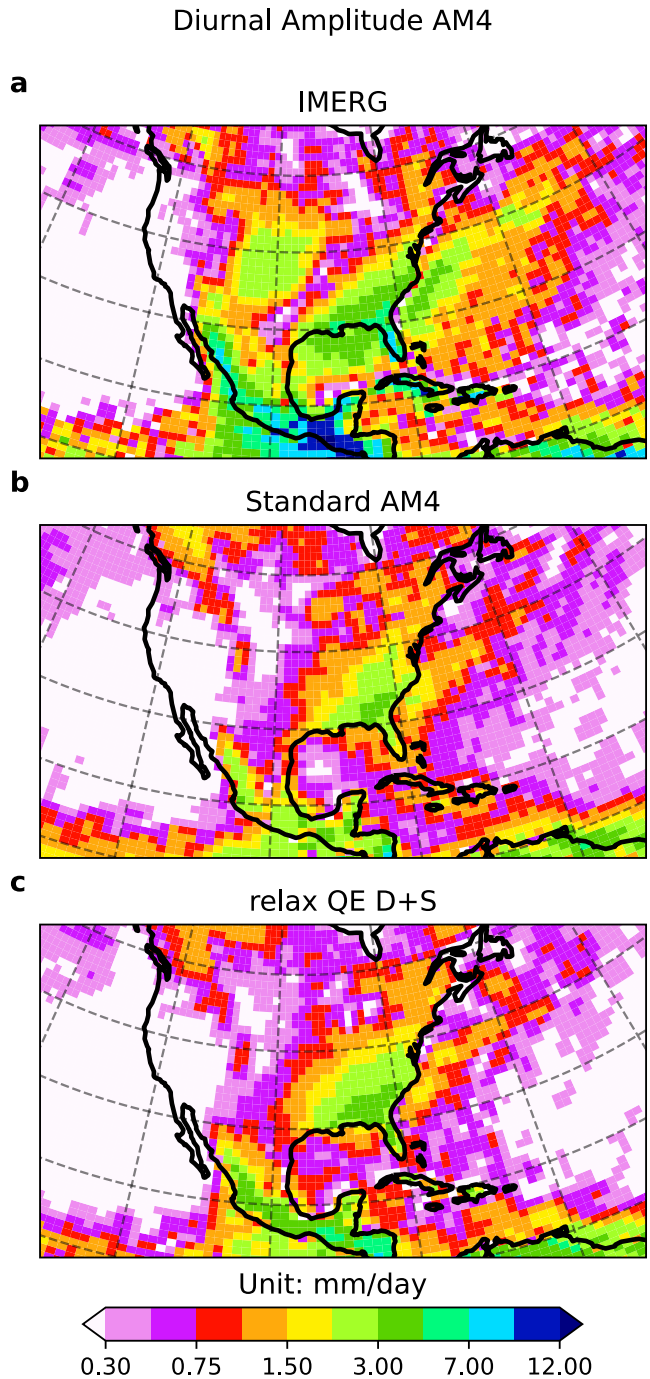

Figure 3. Same as Figure 1 but over the contiguous United States.

African squall lines are not simulated well (Figure 2). The improved diurnal cycles over Asia, Europe, and Africa are consistent and comparable to those reported by Bechtold et al. (2014) (their Figure 5). Although the diurnal cycle of convection in relax QE D+S is significantly improved compared to the observations, the late-night precipitation in relax QE D+S is still underestimated. As mentioned by Bechtold et al. (2014), the late-night precipitation deficit may relate to the missing representation of surface cold pools and upper-level mesoscale lifting.

The total precipitation in AM4 consists of contributions from convective and large-scale parameterizations. We decompose the total precipitation into the convective and large-scale components (Figure 6). Overall, the

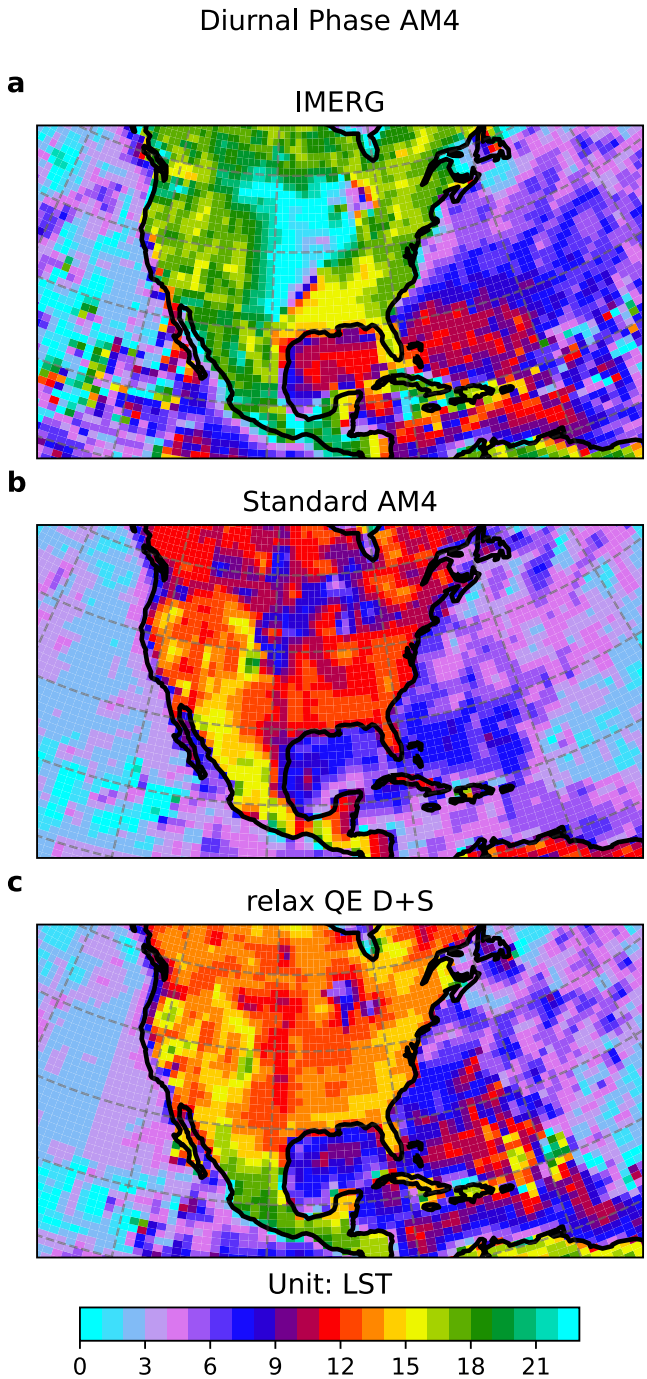

Figure 4. Same as Figure 2 but over the contiguous United States.

convective precipitation peaks a few hours later in relax QE D+S than in standard AM4. The large-scale component is only slightly affected by relax QE D+S. The improved diurnal cycle of total precipitation shown in Figure 5 is mostly contributed by a better representation of the convective precipitation. The observed precipitation minimum around 10a.m. LST (Figure 5) is not captured in either Standard AM4 or relax QE D+S. We do not at present understand this bias, though we note a slight minimum in convective precipitation (Figure 6) around 5a.m. LST, which is a best only slightly delayed with relax QE D+S.

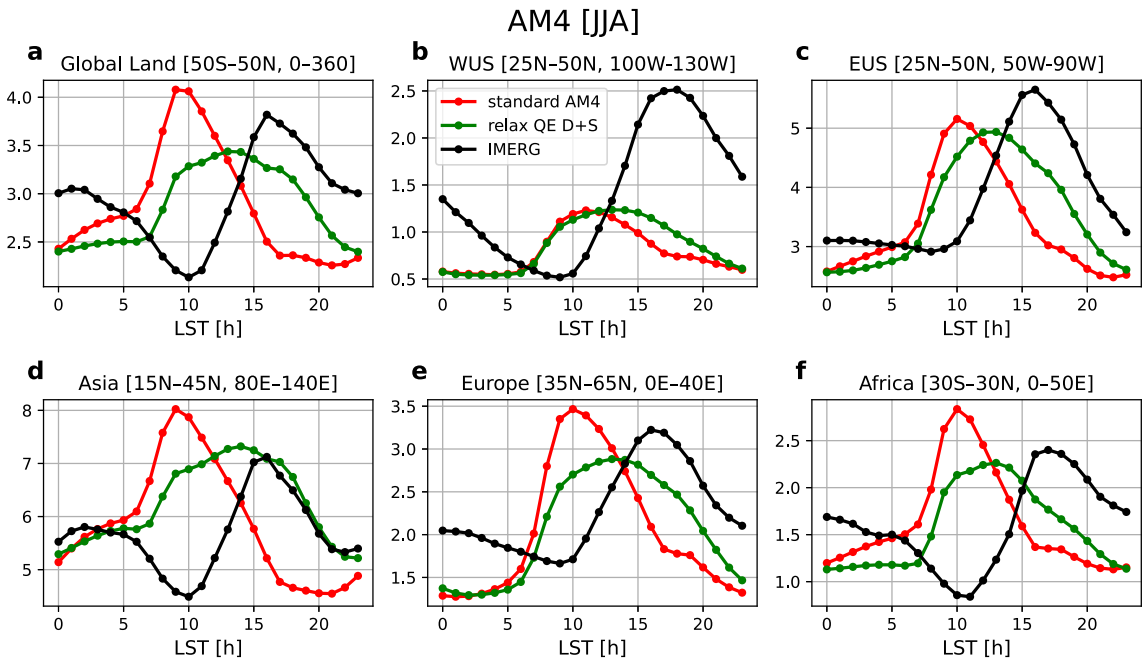

Figure 5. Domain averaged hourly land precipitation (units: mm day^{-1}) averaged from June to August for Standard AM4 (red lines), relax QE D+S (green lines), and IMERG (black lines) over (a) Global Land, (b) Western United States, (c) Eastern United States, (d) Asia, (e) Europe, and (f) Africa.

The phase changes in Figures 1–5 are strongly dominated by including the $\left(\frac{\partial CAPE}{\partial t}\right)_{shal}$ term in Equation 4. There are only small contributions to the phase changes from using relaxed CAPE instead of relaxed CWF in Equations 3 and 4 and from tuning for relax QE D+S.

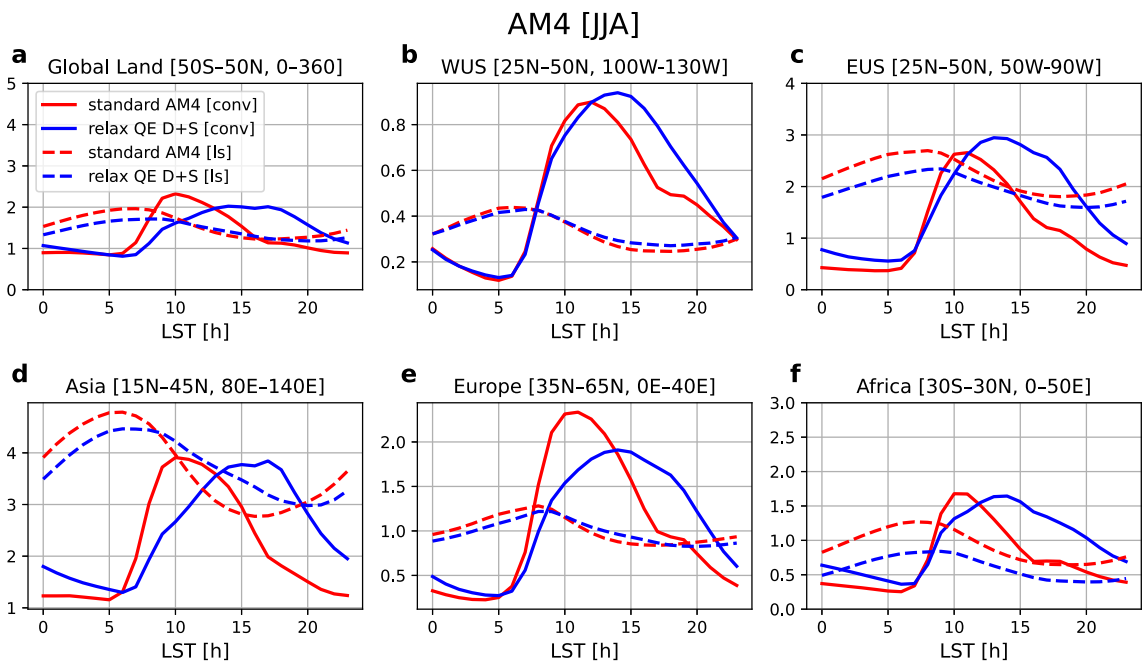

Figure 6. As in Figure 5 except showing a decomposition of the total precipitation into parameterized convection (solid lines) and large scale (dash lines) over the same regions.

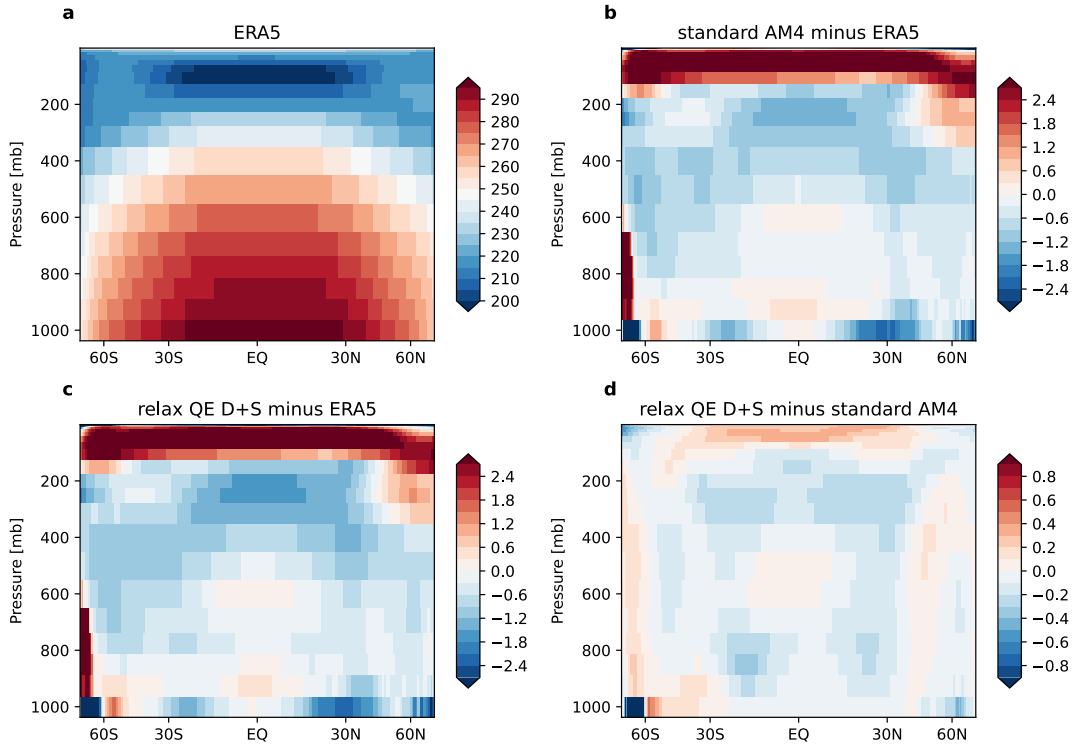

Figure 7. 2001–2014 annual, zonal mean air temperature (units: K) for (a) ERA5, (b) standard AM4 minus ERA5, (c) relax QE D+S minus ERA5, and (d) relax QE D+S minus standard AM4.

3.2. Mean State and Tropical Variability in AM4

Figure 7 compares zonal mean temperature between ERA5, standard AM4 and relax QE D+S. Overall, both standard AM4 and relax QE D+S show colder troposphere but warmer stratosphere than ERA5 (Figures 7b and 7c). In the tropics, standard AM4 is mostly warmer in the troposphere but colder in the stratosphere than relax QE D+S (Figure 7d). Temperature changes from replacing CWF in Standard AM4 with CAPE in the relaxation terms in Equations 3 and 4 are similar in pattern, larger in magnitude, but opposite in sign to those in Figure 7d. Temperature changes associated with the $\left(\frac{\partial CAPE}{\partial t}\right)_{shal}$ term in Equation 4 largely oppose those from replacing CWF with CAPE in the relaxation, as do tuning changes to obtain relax QE D+S. (These intermediate changes are not shown.)

Relax QE D+S slightly increased the cold biases in the upper troposphere compared to standard AM4, but the additional bias at ∼200 hPa is at most around 0.3 degree Celsius. We regard that as acceptable, given the large improvement in the precipitation diurnal cycle. The shortwave and longwave TOA fluxes with relax QE D+S are close to those in standard AM4, evident in Figures 8 and 9. We note that using relax QE D+S shifts the balance between convective and stratiform precipitation in the tropics (from standard AM4 to relax QE D+S, convective precipitation decreases from 2.32 to 1.80 mm day^{-1} while stratiform precipitation increases from 1.20 to 1.77 mm day^{-1}). The vertical profiles of heating differ for convective and stratiform precipitation, and this is likely a factor in the change in the tropical temperature profile with relax QE D+S. The bias could probably be tuned, based on Figure 3 of Zhao et al. (2018b), which shows the tropical upper troposphere cold bias is sensitive to lateral mixing rate in AM4 and that decreasing the lateral mixing rate reduces the cold biases. Overall tuning for AM4 considers many aspects of the circulation, so optimal tuning for upper tropospheric temperature by itself has not been applied.

Outgoing longwave radiation (OLR) in standard AM4 and relax QE D+S are overall similar to CERES-EBAF observations with some regional differences (Figure 8). Compared to standard AM4, relax QE D+S shows enhanced OLR over tropical ocean but reduced OLR over land, with the global mean OLR in relax QE D+S is slightly greater than that in standard AM4 (Figure 8d). The absorbed shortwave radiation (SWABS) patterns are

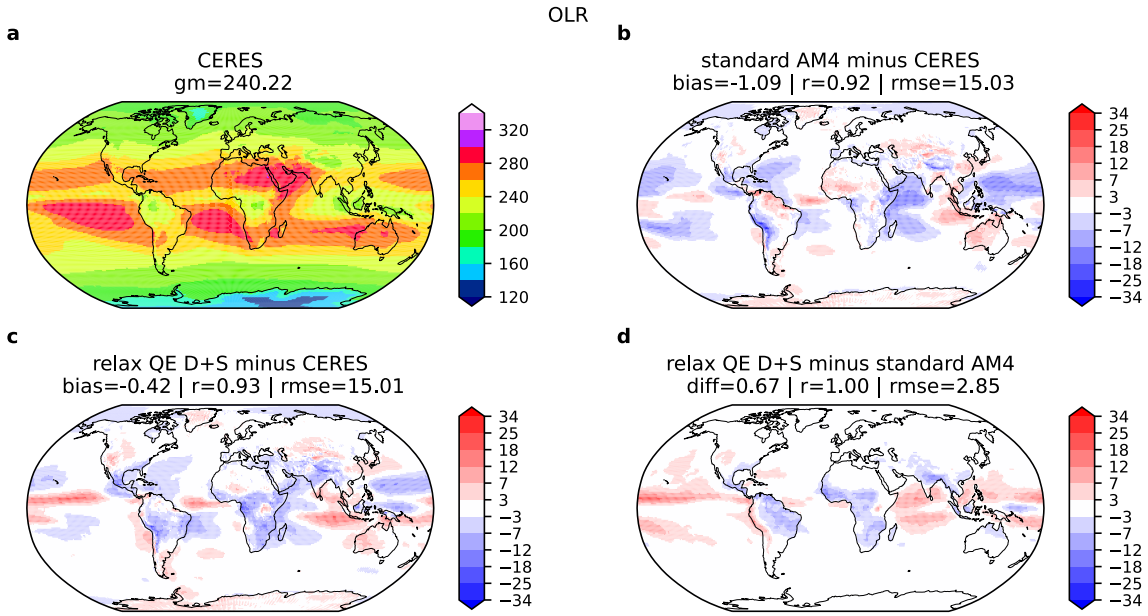

Figure 8. 2001–2014 annual mean OLR (units: W m^{-2}) for (a) CERES EBAF, (b) standard AM4 minus CERES EBAF, (c) relax QE D+S minus CERES EBAF, and (d) relax QE D+S minus standard AM4. Bias (or difference), correlation coefficient, and root mean square error are listed.

also similar between standard AM4 and relax QE D+S, but relax QE D+S also has slightly greater global mean SWABS than standard AM4 (Figure 9). As a result, the energy imbalance at TOA does not change much between standard AM4 and relaxed QE D+S. In addition, standard AM4 and relax QE D+S show similar spatial patterns of mean precipitation, with global mean precipitation in both experiments greater than GPCP (Figure 10). The precipitation intensity distribution is almost identical between standard AM4 and relax QE D+S in the tropics, northern hemisphere mid-latitudes, and southern hemisphere mid-latitudes (Figure 11). The precipitation intensity distribution also remains nearly unchanged between standard AM4 and relax QE D+S when land and ocean are considered separately (not shown), indicating that the new non-equilibrium closure does not affect the overall precipitation statistics. Moreover, the tropical wave spectra analyses show only small changes between

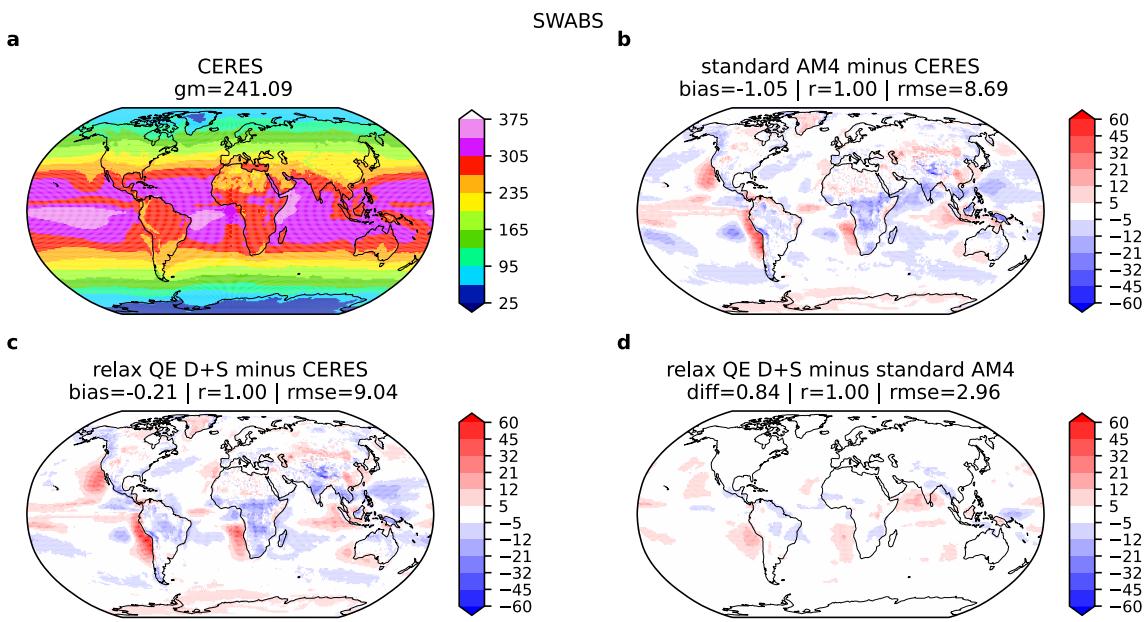

Figure 9. Same as Figure 8 but for SW radiation at TOA (units: W m^{-2}).

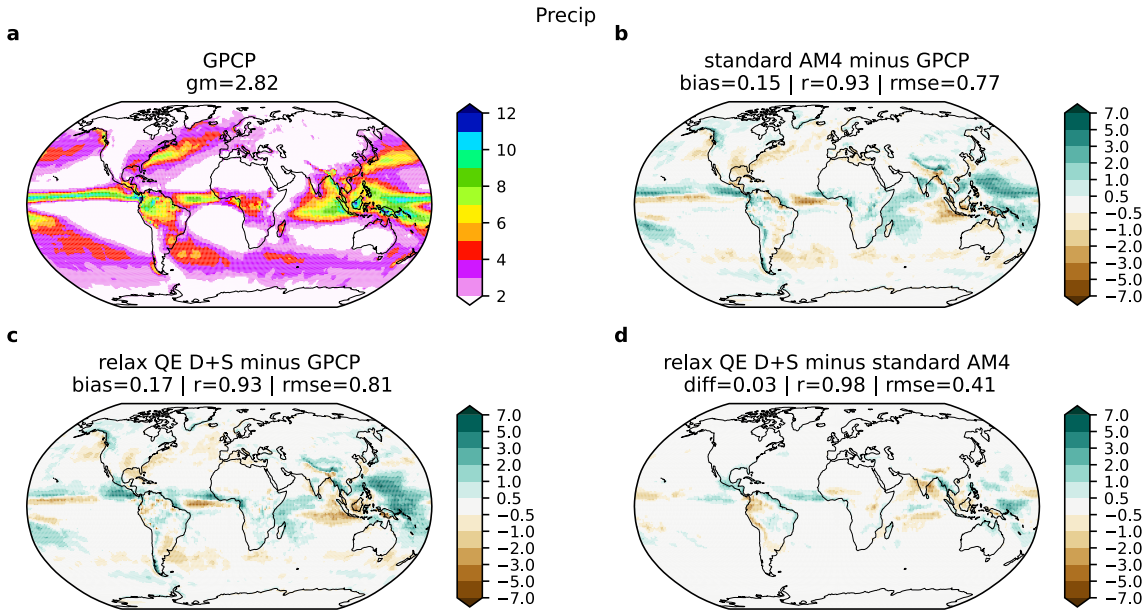

Figure 10. 2001–2014 annual mean precipitation (units: mm day^{-1}) for (a) GPCP, (b) relax QE D+S minus GPCP, (c) relax QE D+S minus GPCP, and (d) relax QE D+S minus standard AM4. Bias (or difference), correlation coefficient, and root mean square error are listed.

standard AM4 and relax QE D+S (Figure 12). Compared to observations, the Kelvin wave is weak in both standard AM4 and relax QE D+S. The strength of Kelvin waves and other behaviors of the tropical wave spectrum have been related to convective entrainment, for example, Figure S1 in Zhao et al. (2018b), as well as the convective closure and triggers (Benedict et al., 2013).

We also conducted idealized experiments with uniform SST warming by 2K to examine the "Cess sensitivity" (Cess et al., 1990), which is computed by examining the change in net TOA flux in response to uniform 2K ocean warming. We found that relax QE D+S yields a Cess sensitivity of 0.54–0.55 K W^{-1} m^2, which is very similar to the value (0.56–0.57 K W^{-1} m^2) reported by Zhao et al. (2018a), indicating that the implementation of the revised closure has little impact on the model's global mean radiative response to uniform SST warming.

3.3. Non-Equilibrium Convection in CM4

Model configurations that are apparently successful in uncoupled simulations do not always withstand coupling without deterioration of major simulation characteristics. For this reason, we briefly compare results between PI-Control and PI Relax QE D+S using CM4. Figure 13c shows the PI Relax QE D+S using non-equilibrium convection is, like the CM4 PI-Control, nearly in energy balance. CM4 PI-Control is described in detail in Held

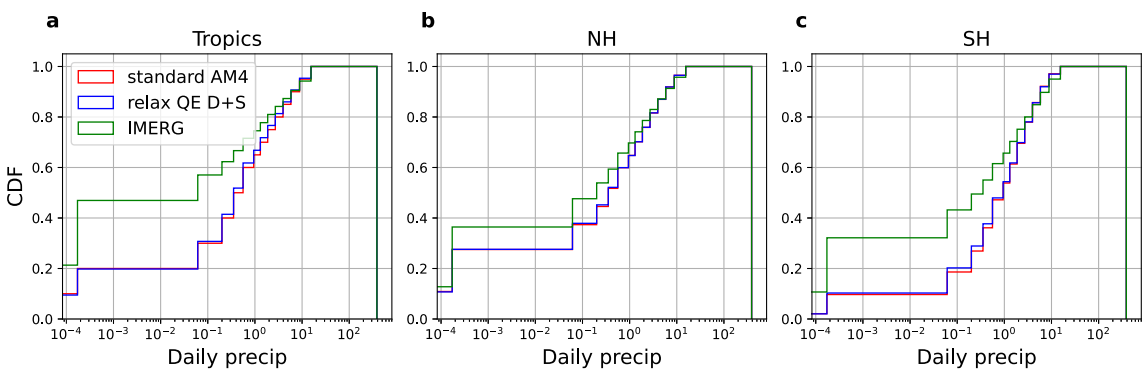

Figure 11. Cumulative distribution of precipitation over (a) Tropics (30°S–30°N), (b) Northern Hemisphere Mid-latitude (30°N–60°N), and (c) Southern Hemisphere Mid-latitude (60°S–30°S). Red curves for standard AM4, Blue for relax QE D+S, and Green for IMERG.

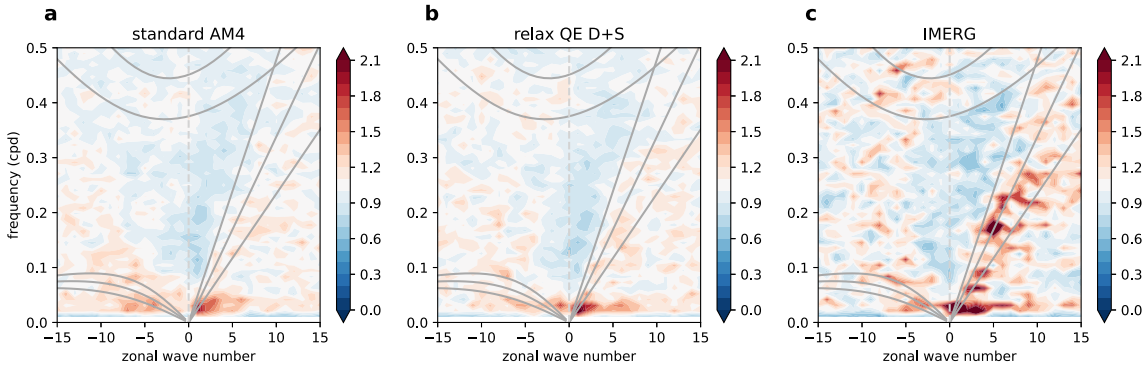

Figure 12. Wave spectra from (a) standard AM4, (b) relax QE D+S and (c) IMERG.

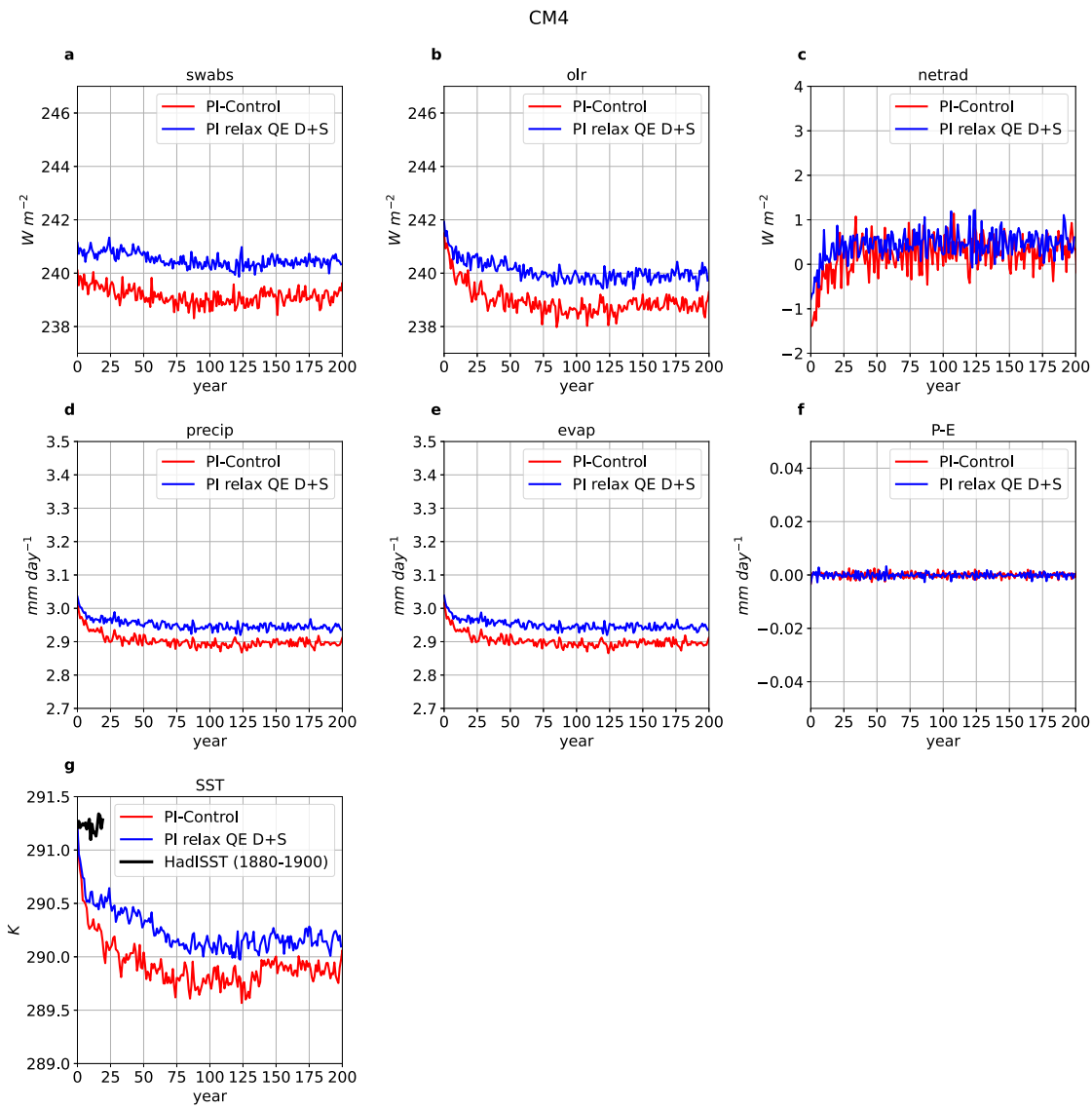

Figure 13. Time series of global, annual-mean (a) SWABS (i.e., SW downward at TOA minus SW upward at TOA); (b) OLR, (c) net radiation at TOA, (d) precipitation, (e) evaporation, (f) precipitation minus evaporation, (g) SST. Red solid lines are for PI-Control, while blue solid curves are for PI Relax QE D+S. The black line in (g) shows HadISST for the 1880–1900 PI period.

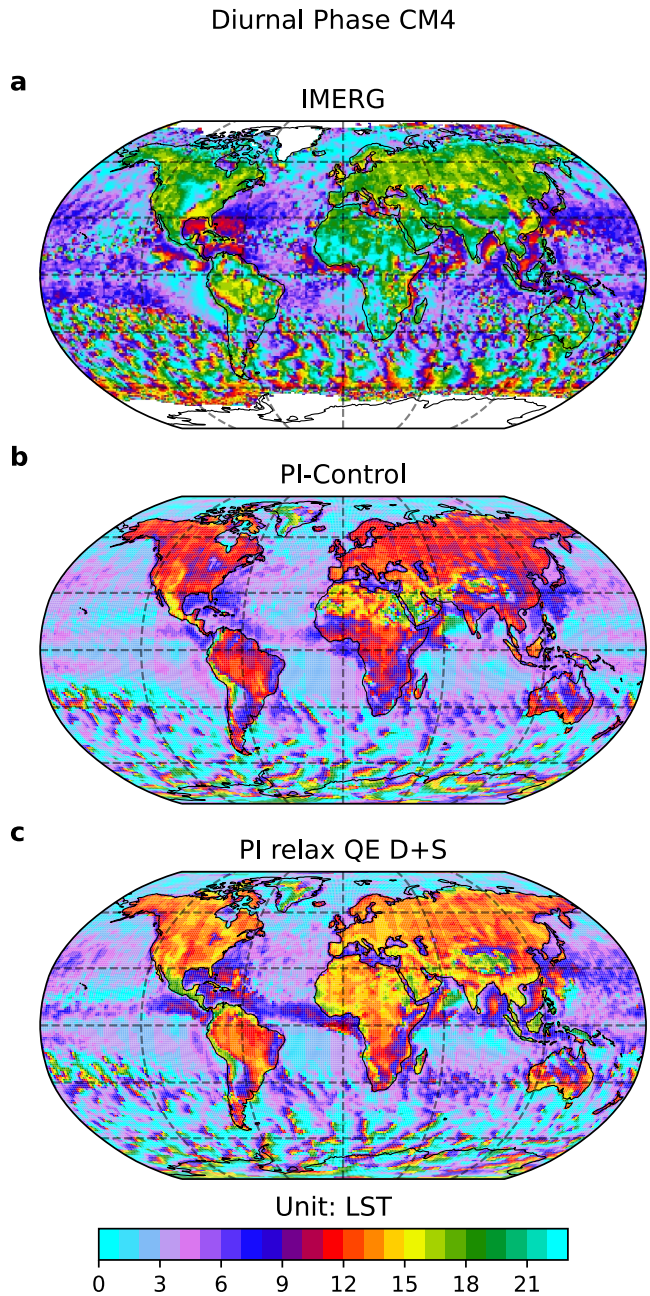

Figure 14. Same as Figure 2 but for the ocean-atmosphere coupled simulations using CM4.

et al. (2019), where it is shown that the imbalance is small enough to allow for CM4 to be used for many climate applications. Observations do not exist for the PI shortwave and longwave components, which must balance each other over extended periods. Figure 13g includes annual mean SST for the 1880–1900 PI period from the Hadley Centre Sea Ice and Sea Surface Temperature (HadISST) data set (Rayner et al., 2003), with PI Relax QE D+S agreeing more closely than PI-Control with the HadISST estimates. The 2001–2014 CERES EBAF TOA SWABS and OLR are 241.0 and 240.2 W m^{-2}, respectively. Forcing from increasing greenhouse gases from PI to present-day (PD) has likely decreased PD OLR from its PI value, so it is likely that PI-Control OLR, which settles around 239 W m^{-2} is less realistic than the PI Relax QE D+S value, which is about 1 W m^{-2} larger. Shortwave feedbacks in response to anthropogenic forcing have likely resulted in PI and PD SWABS differing, though it is difficult to assess this quantitatively, other than to note that SWABS and OLR should balance in PI even as they are out of balance in PD as a consequence of anthropogenic forcing (Figure 13).

Figure 14 shows that the improvements in the diurnal cycle of precipitation with relax QE D+S in AM4 are also evident in CM4. Biases in the diurnal precipitation cycle are reduced by several hours over most land areas, with improvements over many ocean regions as well.

4. Summary

In this study, a new convective closure on the mass flux for deep convection is implemented in GFDL climate models AM4 (atmosphere-only simulations) and CM4 (ocean-atmosphere coupled simulations). The new convective closure is CAPE based and assumes a relaxed quasi-equilibrium between deep convection, shallow convection and non-convective processes (large-scale advection, surface fluxes, radiative transfer, eddy diffusion).

Over land, this new closure improves the diurnal cycle of precipitation with the diurnal phase biases reduced by half. The diurnal cycle of precipitation over ocean is also improved to some extent. This indicates that shallow convection is key to delaying deep convection over land where boundary layer properties (to which shallow convection responds) change rapidly and plays a nonnegligible role in the presence of relatively slow-varying surface conditions over some ocean regions. The revised diurnal cycle of precipitation has implications for weather forecasts of the development and propagation of individual convective systems. Future studies can investigate this in more detail.

Comparisons of the performance in AM4 and CM4 with the new convective closure against IMERG observations indicate that there is still room for improvement in simulating the diurnal cycle of precipitation during boreal summer. Future work may incorporate stochastic entrainment and effects from cold pools. One potential approach for parameterizing cold pools is to make the entrainment rate dependent on the mass flux from downdrafts and surface heat flux as illustrated in Suselj et al. (2019).

Appendix A

Donner and Phillips (2003) (their Figs. 1 and 2) show that CAPE is not in quasi-equilibrium at sub-diurnal time scales but instead changes following temperature and moisture changes in the planetary boundary layer:

$$\frac{\partial CAPE}{\partial t} \cong (\partial_t CAPE)_{BL} \leq \left(\frac{\partial CAPE}{\partial t}\right)_{nc} \tag{A1}$$

$(\partial_t CAPE)_{BL}$ is the total change in CAPE due to changes in PBL temperature and moisture by all physical processes, including convection, and $\left(\frac{\partial CAPE}{\partial t}\right)_{nc}$ is the CAPE change due to non-convective processes, for example, large-scale advection and surface fluxes. In Equation A1, the evolution of CAPE is controlled primarily by the PBL (Donner and Phillips (2003), their Fig. 1).

The failure of quasi-equilibrium,

$$\frac{\partial CAPE}{\partial t} \ll \left(\frac{\partial CAPE}{\partial t}\right)_{nc} \tag{A2}$$

to hold at sub-diurnal time scales has been compensated for by relaxing non-convective CAPE changes toward a threshold CAPE over a time of multiple hours, Equation 3. Donner and Phillips (2003) (their Fig. 5) show that convective heat sources obtained by requiring convective tendencies to balance relaxed non-convective tendencies still agree rather poorly with convective heat sources diagnosed from observations. Accordingly, relaxed quasi-equilibrium for deep convection is augmented by a non-equilibrium term:

$$\left(\frac{\partial CAPE}{\partial t}\right)_{deep} = -\frac{CAPE - CAPE_0}{\tau} + \left(\frac{\partial CAPE}{\partial t}\right)_{non-equil} \tag{A3}$$

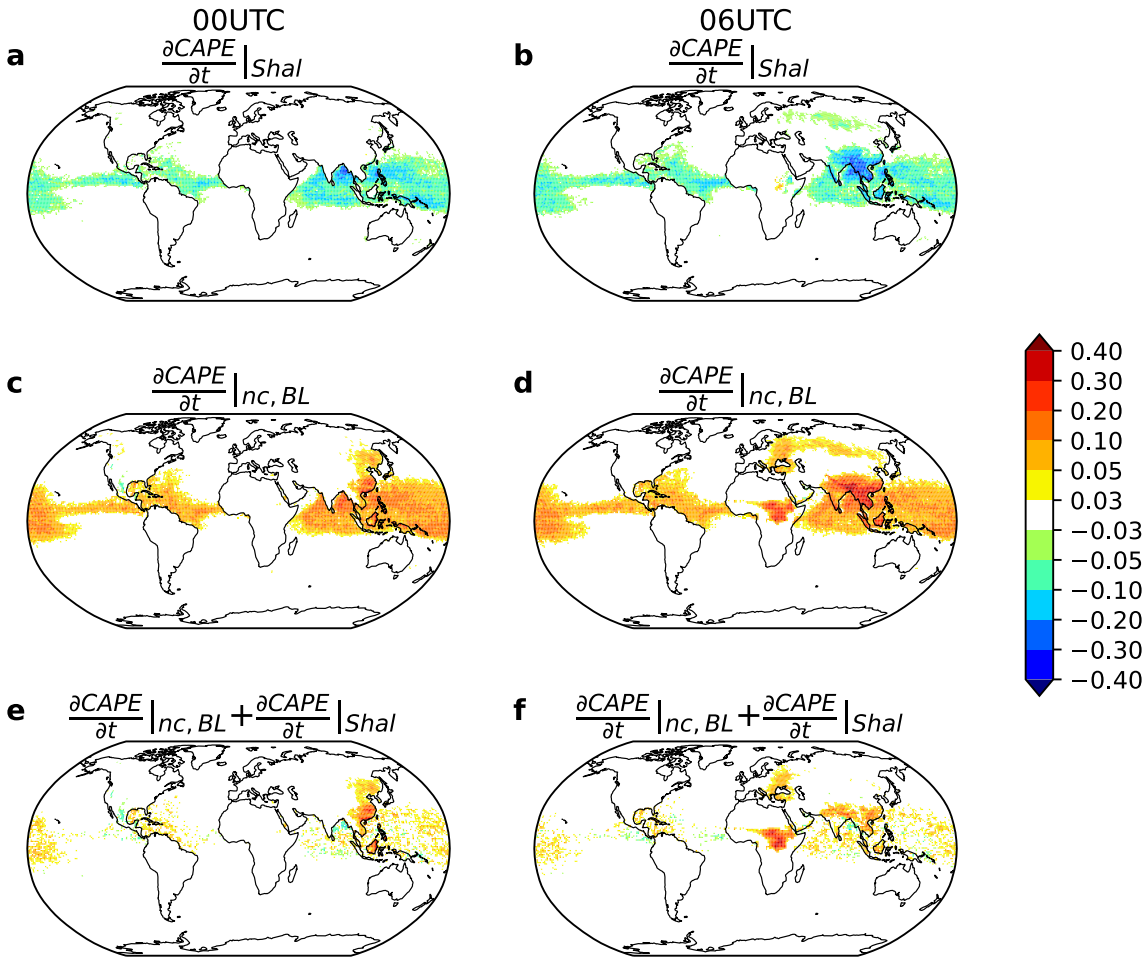

Figure A1. CAPE tendency due to shallow convection (panels a and b), CAPE tendency due to non-convective PBL processes (panels c and d), and the sum of them (panels e and f), retrieved from relax QE D+S. The units for CAPE tendency are J kg^{-1} s^{-1}. The left column is at 00 UTC and the right column is at 06 UTC.

Analysis of non-convective tendencies of temperature and water vapor mixing ratio in Donner and Phillips (2003) (their Fig. 7) suggests:

$$\left(\frac{\partial CAPE}{\partial t}\right)_{non-equil} = \alpha\left(\frac{\partial CAPE}{\partial t}\right)_{nc,BL} \tag{A4}$$

where α is a proportionality constant between 0 and 1, tending toward 1 with increasing non-convective PBL CAPE tendencies. Equation A4 is very similar to Eq. (14) in Bechtold et al. (2014).

Note that, for $\alpha = 1$, the non-equilibrium convective closures Equations 4, A3 and A4 are identical if shallow CAPE tendencies are equal to the negative of the CAPE tendencies from non-convective PBL processes. Physically, this corresponds to shallow convection equilibrating non-convective PBL CAPE changes. In relax QE D+S, this holds to a limited degree. Figures A1 and A2 show global patterns of instantaneous CAPE tendencies from shallow convection, non-convective PBL processes, and the sum of these tendencies composited four times daily from relax QE D+S. Non-convective CAPE tendencies are generally positive, driven by surface heat and moisture fluxes, which respond strongly over land to the diurnal cycle in surface shortwave absorbed radiation. Less frequently, this tendency can be negative and of smaller magnitude, for example, during nocturnal PBL cooling, for example, Figure A1c over Mexico. CAPE tendencies from shallow convection do not fully equilibrate non-convective PBL

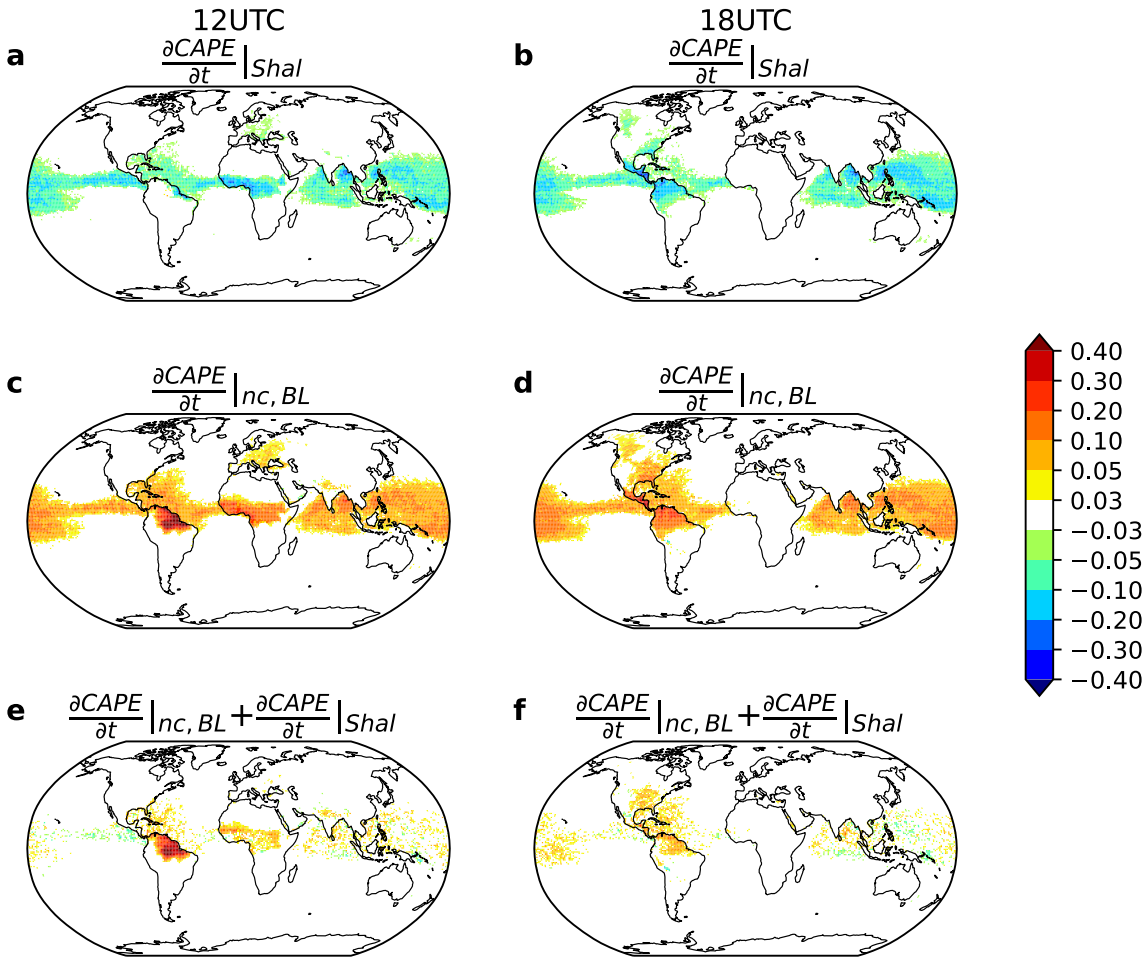

Figure A2. Same as Figure A1 but the left column is at 12 UTC and the right column is at 18 UTC. The units for CAPE tendency are J kg^{-1} s^{-1}.

CAPE changes, and this is especially true over land when surface heating is most pronounced during the diurnal cycle (Figures A1e, A1f and A2e, A2f).

A CAPE based non-equilibrium closure based on Equations A3 and A4 with $\alpha = 1$ is referred to as D PBL CAPE Control. Figures A3a–A3c show the base mass fluxes from a relax QE D+S integration. The base mass fluxes are also calculated from a diagnostic call to D PBL CAPE Control closure in this integration. Figures A3d–A3f show the differences between the base mass fluxes diagnosed from the D PBL CAPE Control closure and those from relax QE D+S. In areas where relax QE D+S base mass fluxes are large and shallow CAPE tendencies do not equilibrate non-convective PBL CAPE tendencies in Figures A1 and A2, the diagnosed D PBL CAPE Control base mass fluxes are less in Figure A3. In regions with smaller relax QE D+S base mass fluxes, the D PBL CAPE Control mass fluxes can be larger. These regions do not support intense convection, and a wider range non-convective PBL CAPE tendencies likely occur. The sum $\left(\frac{\partial CAPE}{\partial t}\right)_{shal} + \left(\frac{\partial CAPE}{\partial t}\right)_{nc,BL}$ in these regions is often small (Figures A1e, A1f and A2e, A2f).

Data Availability Statement

The standard AM4 and CM4 code can be found at https://github.com/NOAA-GFDL/AM4 and https://github.com/NOAA-GFDL/CM4. The code for non-equilibrium convection can be found at https://zenodo.org/records/10709307 (Zhang, 2024). IMERG data sets are from Huffman et al. (2023). GPCP version 3.2 is from Huffman et al. (2022). CERES EBAF data can be found at https://ceres.larc.nasa.gov/data/ (NASA/LARC/SD/ASDC, 2019). ERA5 data is from Hersbach et al. (2023).

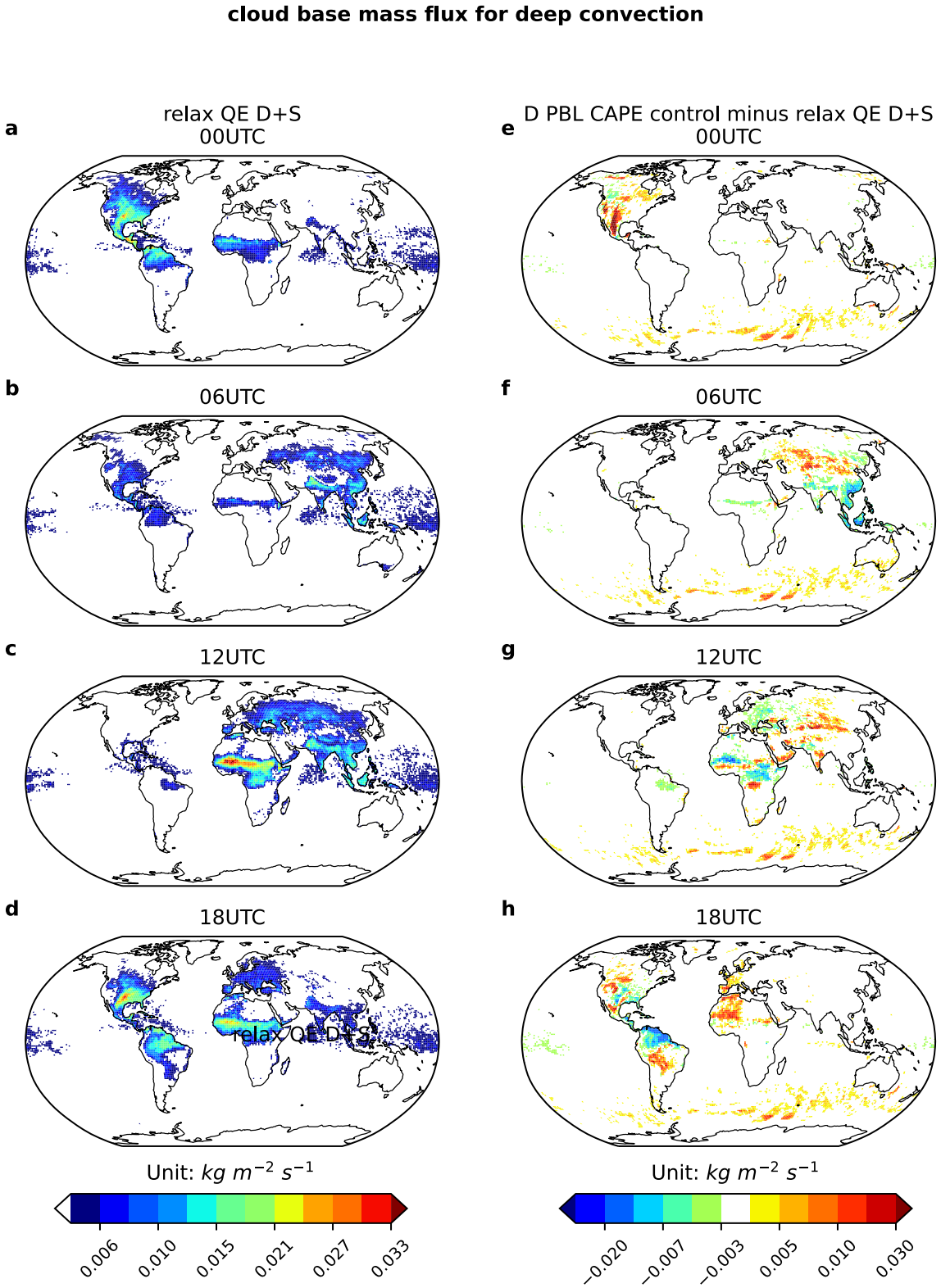

Figure A3. Cloud base mass flux computed from relax QE D+S (panels a–d), and the difference of cloud base mass flux between D PBL CAPE control and relax QE D+S (panels e–h) composited at 00, 06, 12, and 18 UTC. The units for cloud base mass flux are kg m^{-2} s^{-1}.

Acknowledgments
We thank Baoqiang Xiang and Wenhao Dong for their comments on the initial draft of this work. We are grateful to the three anonymous reviewers for their valuable comments and insightful suggestions. Support for this research was provided by the NOAA Climate Program Office through Climate Process Team 140Y8R1ES2/24P01, "From Boundary Layer to Deep Convection: The Multiplume Eddy Diffusivity/Mass Flux Fully Unified Parameterization." This report was prepared by Bosong Zhang under award NA23OAR4320198 from the National Oceanic and Atmospheric Administration, U.S. Department of Commerce. The statements, findings, conclusions, and recommendations are those of the author(s) and do not necessarily reflect the views of the National Oceanic and Atmospheric Administration, or the U.S. Department of Commerce.

References

Anderson, J. L., Balaji, V., Broccoli, A. J., Cooke, W. F., Delworth, T. L., Dixon, K. W., et al. (2004). The new GFDL global atmosphere and land model AM2–LM2: Evaluation with prescribed SST simulations. *Journal of Climate*, *17*(24), 4641–4673.

Arakawa, A., & Schubert, W. H. (1974). Interaction of a cumulus cloud ensemble with the large-scale environment, Part I. *Journal of the Atmospheric Sciences*, *31*(3), 674–701. https://doi.org/10.1175/1520-0469(1974)031<0674:ioacce>2.0.co;2

Bechtold, P., Köhler, M., Jung, T., Doblas-Reyes, F., Leutbecher, M., Rodwell, M. J., et al. (2008). Advances in simulating atmospheric variability with the ECMWF model: From synoptic to decadal time-scales. *Quarterly Journal of the Royal Meteorological Society: A Journal of the Atmospheric Sciences, Applied Meteorology and Physical Oceanography*, *134*(634), 1337–1351. https://doi.org/10.1002/qj.289

Bechtold, P., Semane, N., Lopez, P., Chaboureau, J.-P., Beljaars, A., & Bormann, N. (2014). Representing equilibrium and nonequilibrium convection in large-scale models. *Journal of the Atmospheric Sciences*, *71*(2), 734–753. https://doi.org/10.1175/jas-d-13-0163.1

Benedict, J. J., Maloney, E. D., Sobel, A. H., Frierson, D. M., & Donner, L. J. (2013). Tropical intraseasonal variability in version 3 of the GFDL atmosphere model. *Journal of Climate*, *26*(2), 426–449. https://doi.org/10.1175/jcli-d-12-00103.1

Bretherton, C. S., McCaa, J. R., & Grenier, H. (2004). A new parameterization for shallow cumulus convection and its application to marine subtropical cloud-topped boundary layers. Part I: Description and 1D results. *Monthly Weather Review*, *132*(4), 864–882. https://doi.org/10.1175/1520-0493(2004)132<0864:anpfsc>2.0.co;2

Cess, R. D., Potter, G., Blanchet, J., Boer, G., Del Genio, A., Deque, M., et al. (1990). Intercomparison and interpretation of climate feedback processes in 19 atmospheric general circulation models. *Journal of Geophysical Research*, *95*(D10), 16601–16615. https://doi.org/10.1029/jd095id10p16601

Christopoulos, C., & Schneider, T. (2021). Assessing biases and climate implications of the diurnal precipitation cycle in climate models. *Geophysical Research Letters*, *48*(13), e2021GL093017. https://doi.org/10.1029/2021GL093017

Dai, A., Giorgi, F., & Trenberth, K. E. (1999). Observed and model-simulated diurnal cycles of precipitation over the contiguous United States. *Journal of Geophysical Research*, *104*(D6), 6377–6402. https://doi.org/10.1029/98jd02720

Davies, L., Plant, R., & Derbyshire, S. (2013). Departures from convective equilibrium with a rapidly varying surface forcing. *Quarterly Journal of the Royal Meteorological Society*, *139*(676), 1731–1746. https://doi.org/10.1002/qj.2065

Del Genio, A. D., & Wu, J. (2010). The role of entrainment in the diurnal cycle of continental convection. *Journal of Climate*, *23*(10), 2722–2738. https://doi.org/10.1175/2009jcli3340.1

Dong, W., Krasting, J. P., & Guo, H. (2023). Analysis of precipitation diurnal cycle and variance in multiple observations, CMIP6 models, and a series of GFDL-AM4. 0 simulations. *Journal of Climate*, *36*(24), 8637–8655. https://doi.org/10.1175/jcli-d-23-0268.1

Dong, W., Zhao, M., Ming, Y., Krasting, J. P., & Ramaswamy, V. (2023). Simulation of United States mesoscale convective systems using GFDL's new high-resolution general circulation model. *Journal of Climate*, *36*(19), 6967–6990. https://doi.org/10.1175/jcli-d-22-0529.1

Donner, L. J. (2024). Deep convection and convective clouds. *Fast Processes in Large-Scale Atmospheric Models*, *121*.

Donner, L. J., & Phillips, V. T. (2003). Boundary layer control on convective available potential energy: Implications for cumulus parameterization. *Journal of Geophysical Research*, *108*(D22), 4701. https://doi.org/10.1029/2003jd003773

Donner, L. J., Seman, C. J., Hemler, R. S., & Fan, S. (2001). A cumulus parameterization including mass fluxes, convective vertical velocities, and mesoscale effects: Thermodynamic and hydrological aspects in a general circulation model. *Journal of Climate*, *14*(16), 3444–3463. https://doi.org/10.1175/1520-0442(2001)014<3444:acpimf>2.0.co;2

Donner, L. J., Wyman, B. L., Hemler, R. S., Horowitz, L. W., Ming, Y., Zhao, M., et al. (2011). The dynamical core, physical parameterizations, and basic simulation characteristics of the atmospheric component AM3 of the GFDL global coupled model CM3. *Journal of Climate*, *24*(13), 3484–3519. https://doi.org/10.1175/2011jcli3955.1

Emanuel, K. A. (1991). A scheme for representing cumulus convection in large-scale models. *Journal of the Atmospheric Sciences*, *48*(21), 2313–2329. https://doi.org/10.1175/1520-0469(1991)048<2313:asfrcc>2.0.co;2

Fletcher, J. K., & Bretherton, C. S. (2010). Evaluating boundary layer–based mass flux closures using cloud-resolving model simulations of deep convection. *Journal of the Atmospheric Sciences*, *67*(7), 2212–2225. https://doi.org/10.1175/2010jas3328.1

Fuchs, Ž., & Raymond, D. J. (2007). A simple, vertically resolved model of tropical disturbances with a humidity closure. *Tellus A: Dynamic Meteorology and Oceanography*, *59*(3), 344–354. https://doi.org/10.3402/tellusa.v59i3.14988

Gerard, L., Piriou, J.-M., Brožková, R., Geleyn, J.-F., & Banciu, D. (2009). Cloud and precipitation parameterization in a meso-gamma-scale operational weather prediction model. *Monthly Weather Review*, *137*(11), 3960–3977. https://doi.org/10.1175/2009mwr2750.1

Held, I., Guo, H., Adcroft, A., Dunne, J., Horowitz, L., Krasting, J., et al. (2019). Structure and performance of GFDL's CM4. 0 climate model. *Journal of Advances in Modeling Earth Systems*, *11*(11), 3691–3727. https://doi.org/10.1029/2019ms001829

Hersbach, H., Bell, B., Berrisford, P., Biavati, G., Horányi, A., Muñoz Sabater, J., et al. (2023). ERA5 hourly data on single levels from 1940 to present [Dataset]. *Copernicus Climate Change Service (C3S) Climate Data Store (CDS)*. https://doi.org/10.24381/cds.adbb2d47

Hersbach, H., Bell, B., Berrisford, P., Hirahara, S., Horányi, A., Muñoz-Sabater, J., et al. (2020). The ERA5 global reanalysis. *Quarterly Journal of the Royal Meteorological Society*, *146*(730), 1999–2049. https://doi.org/10.1002/qj.3803

Hirons, L., Inness, P., Vitart, F., & Bechtold, P. (2013). Understanding advances in the simulation of intraseasonal variability in the ECMWF model. Part I: The representation of the MJO. *Quarterly Journal of the Royal Meteorological Society*, *139*(675), 1417–1426. https://doi.org/10.1002/qj.2060

Huffman, G., Behrangi, A., Bolvin, D., & Nelkin, E. (2022). GPCP Version 3.2 satellite-gauge (SG) combined precipitation data set. In G. J. Huffman, A. Behrangi, D. T. Bolvin, & E. J. Nelkin (Eds.), *Goddard Earth Sciences Data and Information Services Center (GES DISC)*. https://doi.org/10.5067/MEASURES/GPCP/DATA304

Huffman, G. J., Behrangi, A., Bolvin, D. T., & Nelkin, E. J. (2022). GPCP version 3.2 satellite-gauge (SG) combined precipitation data set [Dataset]. In G. J. Huffman, A. Behrangi, D. T. Bolvin, & E. J. Nelkin (Eds.). *Goddard Earth Sciences Data and Information Services Center (GES DISC)*. https://doi.org/10.5067/MEASURES/GPCP/DATA304

Huffman, G. J., Bolvin, D. T., Braithwaite, D., Hsu, K., Joyce, R., Xie, P., & Yoo, S.-H. (2015). NASA global precipitation measurement (GPM) integrated multi-satellite retrievals for GPM (IMERG). In *Algorithm theoretical basis document, version, 4* (p. 30).

Huffman, G. J., Stocker, E. F., Bolvin, D. T., Nelkin, E. J., & Tan, J. (2023). GPM IMERG final precipitation L3 half hourly 0.1 degree x 0.1 degree V07, Greenbelt, MD [Dataset]. *Goddard Earth Sciences Data and Information Services Center (GES DISC)*. https://doi.org/10.5067/GPM/IMERG/3B-HH/07

Jones, T. R., & Randall, D. A. (2011). Quantifying the limits of convective parameterizations. *Journal of Geophysical Research*, *116*(D8), D08210. https://doi.org/10.1029/2010jd014913

Kain, J. S., & Fritsch, J. M. (1993). Convective parameterization for mesoscale models: The Kain-Fritsch scheme. In *The representation of cumulus convection in numerical models* (pp. 165–170). Springer.

Kim, D., Sobel, A. H., Maloney, E. D., Frierson, D. M., & Kang, I.-S. (2011). A systematic relationship between intraseasonal variability and mean state bias in AGCM simulations. *Journal of Climate*, *24*(21), 5506–5520. https://doi.org/10.1175/2011jcli4177.1

Lin, J.-L., Kiladis, G. N., Mapes, B. E., Weickmann, K. M., Sperber, K. R., Lin, W., et al. (2006). Tropical intraseasonal variability in 14 IPCC AR4 climate models. Part I: Convective signals. *Journal of Climate*, *19*(12), 2665–2690. https://doi.org/10.1175/jcli3735.1

Loeb, N. G., Doelling, D. R., Wang, H., Su, W., Nguyen, C., Corbett, J. G., et al. (2018). Clouds and the earth's radiant energy system (CERES) energy balanced and filled (EBAF) top-of-atmosphere (TOA) edition-4.0 data product. *Journal of Climate*, *31*(2), 895–918. https://doi.org/10.1175/jcli-d-17-0208.1

Mapes, B. E. (2000). Convective inhibition, subgrid-scale triggering energy, and stratiform instability in a toy tropical wave model. *Journal of the Atmospheric Sciences*, *57*(10), 1515–1535. https://doi.org/10.1175/1520-0469(2000)057<1515:cisste>2.0.co;2

Moorthi, S., & Suarez, M. J. (1992). Relaxed Arakawa-Schubert. A parameterization of moist convection for general circulation models. *Monthly Weather Review*, *120*(6), 978–1002. https://doi.org/10.1175/1520-0493(1992)120<0978:rasapo>2.0.co;2

NASA/LARC/SD/ASDC. (2019). CERES energy balanced and filled (EBAF) TOA and surface monthly means data in netCDF edition 4.1 [Dataset]. *NASA Langley Atmospheric Science Data Center DAAC*. https://doi.org/10.5067/TERRA-AQUA/CERES/EBAF_L3B.004.1

Neelin, J. D., & Yu, J.-Y. (1994). Modes of tropical variability under convective adjustment and the Madden–Julian oscillation. Part I: Analytical theory. *Journal of the Atmospheric Sciences*, *51*(13), 1876–1894. https://doi.org/10.1175/1520-0469(1994)051<1876:motvuc>2.0.co;2

Pan, D. M., & Randall, D. D. (1998). A cumulus parameterization with a prognostic closure. *Quarterly Journal of the Royal Meteorological Society*, *124*(547), 949–981. https://doi.org/10.1002/qj.49712454714

Petch, J., Brown, A., & Gray, M. (2002). The impact of horizontal resolution on the simulations of convective development over land. *Quarterly Journal of the Royal Meteorological Society: A Journal of the Atmospheric Sciences, Applied Meteorology and Physical Oceanography*, *128*(584), 2031–2044. https://doi.org/10.1256/003590002320603511

Piriou, J.-M., Redelsperger, J.-L., Geleyn, J.-F., Lafore, J.-P., & Guichard, F. (2007). An approach for convective parameterization with memory: Separating microphysics and transport in grid-scale equations. *Journal of the Atmospheric Sciences*, *64*(11), 4127–4139. https://doi.org/10.1175/2007jas2144.1

Raymond, D. J., & Herman, M. J. (2011). Convective quasi-equilibrium reconsidered. *Journal of Advances in Modeling Earth Systems*, *3*(3), M08003. https://doi.org/10.1029/2011ms000079

Rayner, N., Parker, D. E., Horton, E., Folland, C. K., Alexander, L. V., Rowell, D., et al. (2003). Global analyses of sea surface temperature, sea ice, and night marine air temperature since the late nineteenth century. *Journal of Geophysical Research*, *108*(D14), 4407. https://doi.org/10.1029/2002jd002670

Rio, C., Hourdin, F., Grandpeix, J. Y., & Lafore, J. P. (2009). Shifting the diurnal cycle of parameterized deep convection over land. *Geophysical Research Letters*, *36*(7), L07809. https://doi.org/10.1029/2008gl036779

Stirling, A., & Stratton, R. (2012). Entrainment processes in the diurnal cycle of deep convection over land. *Quarterly Journal of the Royal Meteorological Society*, *138*(666), 1135–1149. https://doi.org/10.1002/qj.1868

Stratton, R., & Stirling, A. (2012). Improving the diurnal cycle of convection in GCMs. *Quarterly Journal of the Royal Meteorological Society*, *138*(666), 1121–1134. https://doi.org/10.1002/qj.991

Suselj, K., Kurowski, M. J., & Teixeira, J. (2019). A unified eddy-diffusivity/mass-flux approach for modeling atmospheric convection. *Journal of the Atmospheric Sciences*, *76*(8), 2505–2537. https://doi.org/10.1175/jas-d-18-0239.1

Tao, C., Xie, S., Ma, H. Y., Bechtold, P., Cui, Z., Vaillancourt, P. A., et al. (2024). Diurnal cycle of precipitation over the tropics and central United States: Intercomparison of general circulation models. *Quarterly Journal of the Royal Meteorological Society*, *150*(759), 911–936. https://doi.org/10.1002/qj.4629

Tian, B., Held, I. M., Lau, N. C., & Soden, B. J. (2005). Diurnal cycle of summertime deep convection over North America: A satellite perspective. *Journal of Geophysical Research*, *110*(D8), D08108. https://doi.org/10.1029/2004jd005275

Tiedtke, M. (1989). A comprehensive mass flux scheme for cumulus parameterization in large-scale models. *Monthly Weather Review*, *117*(8), 1779–1800. https://doi.org/10.1175/1520-0493(1989)117<1779:acmfsf>2.0.co;2

Watters, D., Battaglia, A., & Allan, R. P. (2021). The diurnal cycle of precipitation according to multiple decades of global satellite observations, three CMIP6 models, and the ECMWF reanalysis. *Journal of Climate*, *34*(12), 5063–5080. https://doi.org/10.1175/jcli-d-20-0966.1

Xie, S., Wang, Y. C., Lin, W., Ma, H. Y., Tang, Q., Tang, S., et al. (2019). Improved diurnal cycle of precipitation in E3SM with a revised convective triggering function. *Journal of Advances in Modeling Earth Systems*, *11*(7), 2290–2310. https://doi.org/10.1029/2019ms001702

Yano, J. I., & Plant, R. (2012). Finite departure from convective quasi-equilibrium: Periodic cycle and discharge–recharge mechanism. *Quarterly Journal of the Royal Meteorological Society*, *138*(664), 626–637. https://doi.org/10.1002/qj.957

Zhang, B. (2024). Non-equilibrium code [Software]. *Zenodo*. https://doi.org/10.5281/zenodo.10709307

Zhang, G. J. (2002). Convective quasi-equilibrium in midlatitude continental environment and its effect on convective parameterization. *Journal of Geophysical Research*, *107*(D14), ACL12-11–ACL12-16. https://doi.org/10.1029/2001jd001005

Zhang, G. J. (2003). Convective quasi-equilibrium in the tropical western Pacific: Comparison with midlatitude continental environment. *Journal of Geophysical Research*, *108*(D19), 4592. https://doi.org/10.1029/2003jd003520

Zhang, G. J., & McFarlane, N. A. (1995). Sensitivity of climate simulations to the parameterization of cumulus convection in the Canadian climate centre general circulation model. *Atmosphere-Ocean*, *33*(3), 407–446. https://doi.org/10.1080/07055900.1995.9649539

Zhao, M., Golaz, J. C., Held, I., Guo, H., Balaji, V., Benson, R., et al. (2018a). The GFDL global atmosphere and land model AM4. 0/LM4. 0: 1. Simulation characteristics with prescribed SSTs. *Journal of Advances in Modeling Earth Systems*, *10*(3), 691–734. https://doi.org/10.1002/2017ms001208

Zhao, M., Golaz, J. C., Held, I., Guo, H., Balaji, V., Benson, R., et al. (2018b). The GFDL global atmosphere and land model AM4. 0/LM4. 0: 2. Model description, sensitivity studies, and tuning strategies. *Journal of Advances in Modeling Earth Systems*, *10*(3), 735–769. https://doi.org/10.1002/2017ms001209